FINITE ELEMENT BASED ALGORITHM FOR SELF-INDUCED MAGNETIC FIELD APPLICATIONS

K. J. Berry and Subrata Roy
Kettering University
Flint, MI

Paper no. AIAA-2001-0200

FINITE ELEMENT BASED ALGORITHM FOR SELF-INDUCED MAGNETIC FIELD APPLICATIONS

K.J. Berry* and Subrata Roy**
Kettering University, Flint, MI 48504

ABSTRACT

This paper introduces a *loosely-coupled* computational method that combines the Galerkin Finite Element Method (GFEM) and the Least Squares Finite Element Method (LSFEM) that is applicable for self-induced magnetic field engineering applications. The combined Galerkin Least Squares (GLS) algorithm is employed to enhance the theoretical understanding for a fully ionized, single temperature fluid in magnetoplasmadynamic (MPD) thrusters. The computational model addresses the potential understanding of geometric and parametric scales, and predictions of self-induced magnetic effects. Documented results on practical two-dimensional computational domain show the capability of the GLS algorithm under different parametric design conditions.

* Professor and Head, Dept. of Mechanical Engineering, Member
** Assistant Professor, Dept. of Mechanical Engineering, Associate Fellow.

NOMENCLATURE

b_l – Local Magnetic Field (Weber/m^2)
B – Magnetic Field (Weber/m^2)
E – Electric Field (V/m)
h – Enthalpy (J/kg)
J– Current Density (A/m^2)
k – Thermal Conductivity (W/m-K)
p – Pressure (Pa)
R – Gas Constant (J/kg-K)
T – Temperature (K)
V – Velocity (m)
ρ - Density (kg/m^3)
μ_f - Fluid Viscosity (Pa-s)
μ_0 - Permeability of Free Space (W/A-m)
E_c - Electron Charge (c)
I_m - Ion Mass (kg)
H - Hall Parameter($b_l\,\sigma/P_nE_c$)
P_n – Plasma Number Density (ρ/I_m-Particles/m^3)
σ - Electrical Conductivity (mho/m)
ϕ - Voltage (V)
T_e – Thrust (N)
V_e – Exit Velocity (m/s)

Subscripts

0 – reference value
t – tank condition
e – exit condition
el – element

1.0 Introduction

The basic *magnetohydrodynamics* (*MHD)* equations are the Navier-Stokes equations that govern the fluid hydrodynamics [1] and Maxwell's equations that govern the electromagnetics [2]. These equations form the basis of MHD for a moving media and are coupled through viscous and magnetic body forces that may be temperature dependent.

This paper develops a two-dimensional steady state algorithm utilizing a combination of the Galerkin weak statement (GWS) and least squares finite element (LSFEM) methods [3] for MHD applications. The GWS is used to analyze the single fluid Navier-Stokes regime subjected to electromagnetic forces, while the LSFEM solves the electromagnetic Maxwell's equations. This *loosely-coupled* Galerkin and Least Square (GLS) algorithm allows for a very robust and mathematically complete approach. The following sections highlights the theoretical developments for the computational methodology, and presents quantitative documentation of achievable high quality practical MHD solutions.

1.1 Fluid Dynamics Field Equations

To obtain a better understanding of parameters affecting the behavior of MHD related problems, we derive a set of dimensionless equations using the following variables:

$$
\begin{array}{lll}
V^* = \dfrac{V}{V_0}, & T^* = \dfrac{T}{T_0}, & P^* = \dfrac{P - P_t}{P_0} \\
m_f{}^* = \dfrac{m_f}{m_{f\,0}}, & k^* = \dfrac{k}{k_0}, & r^* = \dfrac{r}{r_0} \\
J^* = \dfrac{J}{J_0}, & B^* = \dfrac{B}{B_0}, & E^* = \dfrac{E}{E_0} \\
h^* = \dfrac{h}{h_0}, & \nabla^* = X_0 \bullet \nabla &
\end{array}
$$

All other dimensionless and reference parameters are defined in Appendix A.

The equations for the conservation of momentum and mass for steady compressible MHD flow are expressed in dimensionless vector notation as:

$$
\begin{aligned}
r^*(T^*)\left(\vec{V}^* \bullet \nabla^*\right)\vec{V}^* = -\nabla^* p^* - \left[\nabla \bar{t}^*\right] & \\
- \frac{2}{3\mathrm{Re}} \nabla^* \left[m^*(T^*) \nabla^* \bullet \vec{V}^* \right] & \qquad (1) \\
+ \Delta_0\, \vec{J}^* \times \vec{B}^* & \\
\nabla^* \bullet \left(r^* \vec{V}^* \right) = r^* \nabla^* \bullet \vec{V}^* + \vec{V}^* \nabla^* \bullet r^* = 0 &
\end{aligned}
$$

where the stress tensor $\bar{t}$ is expressed as:

$$
\bar{t}^* = -\frac{m^*(T)}{\mathrm{Re}} \left(\nabla^* \vec{V}^* + \nabla^{*T} \vec{V}^* \right) \qquad (2)
$$

The term $\vec{J}\times\vec{B}$ in (1) represents the electromagnetic body force caused by the interaction of the applied current $\vec{J}$ and the induced magnetic field $\vec{B}$. Similarly, the conservation of energy may be expressed as:

$$
\begin{aligned}
\nabla^* \bullet \left(r^* h^* \vec{V}^* \right) = & -\nabla^* \bullet \vec{q}^* - \Phi_0 \left(\bar{t}^* : \nabla^* \vec{V}^* \right) \\
& + \Pi_0 \left(\vec{V}^* \bullet \nabla^* \right) p^* \\
& + \Psi_0 \vec{E}^* \bullet \vec{J}^*
\end{aligned} \tag{3}
$$

where $\vec{E} \bullet \vec{J}$ represents the Joulean dissipation body force from the interaction of the applied electric field $\vec{E}$ and the applied current field $\vec{J}$.

The appropriate Fourier constitutive law and ideal gas closure relations are:

$$
\begin{aligned}
\vec{q}^* &= -\frac{k^*(T^*)}{Pe} \nabla^* T^* \\
r^* &= \frac{g\, Ma^2}{T^*} \left(\frac{P_t}{P_0} + P^* \right)
\end{aligned} \tag{4}
$$

where *Pe* is the Peclect number and *Ma* is the Mach number.

1.2 Electromagnetic Field Equations

The non-dimensional Maxwell form for steady-state, single fluid assumptions may be derived as:

$$
\begin{aligned}
\nabla^* \bullet \vec{B}^* &= 0 \\
\nabla^* \times \vec{B}^* &= \vec{J}^* \\
\nabla^* \bullet \vec{J}^* &= 0 \\
\nabla^* \times \vec{E}^* &= 0
\end{aligned} \tag{5}
$$

The necessary constitutive relation is expressed as:

$$\vec{J}^{*} = \sigma^{*}(T^{*})\left[\left(\frac{\sigma_0 E_0}{J_0}\right)\vec{E}^{*} + \left(\frac{\sigma_0 V_0 B_0}{J_0}\right)\vec{V}^{*}\times\vec{B}^{*}\right] - H_0\frac{\sigma^{*}}{\rho^{*}}\left(\vec{J}^{*}\times\vec{B}^{*}\right) \tag{6}$$

In (6), Ohm's law relates the current density $\vec{J}$ to the plasma velocity $\vec{V}$, the electric field $\vec{E}$, and the magnetic field $\vec{B}$ with the ion slip terms neglected due to the full ionization assumption. The Hall Parameter H_0 is the product of the electron cyclotron frequency and the electron collision time expressed as:

$$H_0 = \frac{B_0 \sigma_0 I_m}{\rho_0 E_c} \tag{7}$$

where B_0 is the magnitude of the reference magnitude field, I_m is the ion mass, and E_c is the electron charge.

The above coupled equation sets, (1)-(7), can be solved numerically for field variables of velocity $\{v_z^{*}, v_r^{*}\}$, temperature $\{T^{*}\}$, density $\{\rho^{*}\}$, pressure $\{p^{*}\}$, current $\{J_z^{*}, J_r^{*}\}$, voltage $\{\phi^{*}\}$, and induced magnetic field $\{B_\theta^{*}\}$ for a wide range of practical engineering applications. From Appendix A and (1)-(7) it can be seen that primary input variables are the applied reference current I_0, the reference plasma temperature T_0, the reference propellant tank pressure P_t, and Ψ_0 defined as the ratio of electrical input energy to thermal input energy.

2.0 MHD Numerical Implementation

The MHD solution strategy integrates the *Galerkin weak statement (GWS)* to solve the fluid dynamic equations and the *least-squares finite element method (LSFEM)* to solve the electromagnetic equations. Both equation sets provide a coupled solution for all field variables to enhance convergence.

2.1 Galerkin Weak Statement (GWS)

With the unequal velocity-pressure formulation, we assume that the velocity components are interpolated at 'r' nodes, while the pressure is interpolated at 's' nodes, where in general r > s. This representation is required to remove any spurious pressure fields and is similar to the staggered grid approach employed in the finite difference method.

The finite element matrices are developed via Bubnov-Galerkin's weighted residual method. We require that a weighted value of a residual, *R*, be a minimum over the domain, Ω, by employing piece-wise continuous interpolation functions, *N*. With Galerkin's method the weighting or interpolation functions are defined as the element shape functions, N_i. Thus, for each element node, i, we have:

$$\iiint_{\Omega} RN_i \, d\Omega = 0 \; (i = 1, 2, , , n)$$

where for cylindrical coordinate the differential volume is defined as $d\Omega = 2p\, rdrdz$.

Using Galerkin's method along with Green's theorem for integration by parts in 2D, the element matrices always result in a set of non-linear simultaneous equations [4] of the form:

$$[\mathbf{K}]\{U\} = \{F\}$$

where $\{U\} = \{v_z^*, v_r^*, T^*, r^*, p^*\}$ is the global solution vector, $\{F\}$ is the global force vector and [K] is the global stiffness matrix expressed as:

$$[K] = \begin{bmatrix} [K_{11}] & [K_{12}] & [K_{13}] & [K_{14}] & [K_{15}] \\ [K_{12}^T] & [K_{22}] & [K_{23}] & [K_{24}] & [K_{25}] \\ [K_{31}] & [K_{32}] & [K_{33}] & [K_{34}] & [K_{35}] \\ [K_{41}] & [K_{42}] & [K_{43}] & [K_{44}] & [K_{45}] \\ [K_{15}^T] & [K_{25}^T] & [K_{53}] & [K_{54}] & [0] \end{bmatrix}$$

The exact form of the global sub-matrices, $[K_{ij}]$, is provided in Appendix B. In the above stiffness matrix, {N} is the familiar shape function vector with its gradient matrix [B], where $\{B_r\}$ and $\{B_z\}$ are the individual rows corresponding to the radial or axial axis. The superscript 's' in Appendix B corresponds to the pressure degrees-of-freedom.

2.2 Least Square Finite Element Method (LSFEM)

Most problems arising in fluid dynamics, solid mechanics, heat transfer, electromagnetic and other mathematical physics can be recast in the form of first-order systems [5-7]. These systems result in first-order differential equations that are derived from their appropriate conservation and constitutive laws. As such the LSFEM discussed herein requires the minimization of the differential equation residual in the L_2 norm, where $L_2(\Omega)$ denotes the space of square-integrable functions. For a general state vector {u}, where $u_i = u(x_i)$ and $u_j = u(x_j)$, we define on Ω the inner product as:

$$(u_i, u_j) = \int_{\Omega} u_i u_j \, d\Omega, \quad u_i, u_j \in L_2(\Omega),$$

with norm**:**

$$\|u\|_0^2 = (u_i, u_i), \quad u_i \in L_2(\Omega)$$

Consider the following boundary value problem (BVP):

$$\begin{aligned} Lu - f &= 0 \quad in\,\Omega \\ Bu - g &= 0 \quad on\,\Gamma, \end{aligned}$$

where f is a given vector-valued function, B is a boundary operator, g is a given vector-valued function on the boundary that is assumed to be zero, and L is a linear first-order partial differential operator,

$$Lu = A_0 \frac{\partial u}{\partial t} + \sum_{i=1}^{nd} A_i \frac{\partial u}{\partial x_i} + Au \qquad in\,\Omega, t > 0$$
$$B \bullet u = g \quad on\,\Gamma, t \geq 0,$$
$$u = u_0 \quad in\,\Omega, t = 0. \tag{8}$$

In (8), $\Omega \in R^n$ is a bounded domain with a piecewise smooth boundary Γ, and n=2,3 represents space dimensions.

Considering the boundary condition of the BVP and defining an appropriate Sobolev function space, S, the minimization of the residual with respect to unknown vector *u*, leads to the least-squares weak statement [7]:

$$(Lw, Lu) = (Lw, f) \quad \forall w \in S \tag{9}$$

where $\delta u = w$ and $u \in S$.

2.3 Finite Element Discretization

We first discretize the computational domain as a union of finite elements and then introduce an appropriate basis function. Let *'ne'* denote the number of element nodes, *'m'* denote the degrees-of-freedom per node, *{u}* denote a vector containing *'M'* nodal parameter values (M = ne x m), and *{N(x)}* denote the element basis or shape function vector. If equal-order interpolation is assumed for all unknown element variables, we can write the expansion:

$$U(x_i) = \{N(x_i)\}^T \{u\} \tag{10}$$

where $U(x_i)$ is the value of unknown state vector {u} at location x_i. Introducing (10) into the least-squares weak statement (9) results in linear equation system of the form:

$$[K_{el}]\{U\} = \{F\}$$

where {U} is the global vector of nodal values. The global matrix [K] is assembled from the element matrices:

$$
\begin{aligned}
[K_{el}]_b &= \sum_{i=1}^{ne}\sum_{j=1}^{ne}[k(i,j)]_m \\
&= \int_{\Omega_e}\left[L(N_i(x))\right]^T\left[L(N_j(x))\right]\left\{U^{n+1}\right\}d\Omega
\end{aligned}
\tag{11}
$$

where [K_{el}] is a square matrix of size *(b=ne x m)* and [k(i,j)] is a square sub-matrix of size *m* in which $\Omega_e \subset \Omega$ is the domain of the *eth* element. The body force/residual vector {F} is assembled from the element vectors: $\{F_e\} = \int_{\Omega_e}\left[L(N_i(x))\right]^T\left\{f_e + \frac{A_0}{\Delta t}U^n\right\}d\Omega$

in which from (8):

$$
\begin{aligned}
\left[L(N_i(x))\right] &= \frac{A_0}{\Delta t}N_i(x) + \left[A\right]N_i(x) \\
&+ \sum_{i=1}^{nd}\left[A_i\right]\frac{\partial N_i(x)}{\partial x_i}
\end{aligned}
\tag{12}
$$

where $\Delta t = t^{n+1} - t^n$ and *n* denotes the nth time level. The matrix [K] is always symmetric and positive definite (SPD) and thus, iterative robust solution methods may be employed. It is also important to emphasize that there are no weighting or upwind parameters, nor is there any added dissipation, or other non-physical ad-hoc modifications to the system of equations. The LSFEM solves the primary unknown variables in a fully-coupled manner, no splitting or projection (which may lead to convergence difficulties) is involved. Besides the finite element interpolation and the linearization, no other approximation is introduced. Therefore, the method is accurate and robust. In addition, LSFEM allows for the possibility of more system equations than unknown variables.

2.4 Loosely-Coupled GLS Algorithm

The loosely-coupled GLS algorithm is described as follows:

1. Initialize variables.
2. Compute currents, voltages and magnetic fields via LSFEM.
3. Update momentum loads.
4. Compute velocity, temperature, density, and pressure via GFEM.
5. Update thermal properties.
6. If not converged goto 2.
7. Post-process efficiency.
8. Stop.

The algorithm as described is efficient and very robust due to coupling of magnetic and flow variables using a direct wave front solver. The exact form of the LSFEM [A] matrix along with the schematic overview is provided in [8].

3.0 MPD Thruster Simulation

The *magnetoplasmadynamic (MPD)* thruster is being considered as a high power in-space propulsion system to support missions of interest to the NASA Earth Science, Space Science, and Human Exploration and Development of Space Strategic Enterprises. In this robust electric propulsion device arc current is utilized as an ionizer for the gaseous propellant that interacts with the self-induced magnetic field to accelerate the plasma, and produce the required thrust through an inherently unsteady process [9-11]. The MHD equations as presented above (1)-(5) can be used for MPD thruster analysis assuming a single fluid/ single temperature approximation. This implies the plasma to be fully and singly ionized. We also assume the plasma is described by a perfect gas equation of state.

Computational researchers have tried to effectively capture the physics of self-field MPD thrusters [12,13] using two-dimensional time-independent computational fluid dynamics (CFD) model for argon propellant. While finite difference methodology is utilized in [12] to solve the fully ionized MPD equations with ideal gas equation of state, the velocity, pressure, electron-ion temperature and current field solutions in [13] are computed by the finite volume methodology. Results in both these papers were reasonably compared with experimental thrust data.

Numerical solutions reported in [14] included the temporal contributions via a special consideration to the difference between characteristic time scale of fluid-thermal (msec) and electromagnetic (μsec) effects. A detail comparison of thrust versus current curves for various mass flow rates is presented in [15]. These results show a wide variation of numerical solution accuracy for DT series and hot anode thrusters (HAT). Applications of finite volume method in general two-dimensional unsteady plasma dynamics have also been reported by Air Force Research Laboratory researchers [16]. The methodology involves solutions of mass, momentum, electron and ion energy, radiation energy density, magnetic induction and elastic stress equations in arbitrary Lagrangian/Eulerian (ALE) coordinate. A recent publication [17] documents the application of this code for applied-field MPD thrusters. However, the solution stability and boundary condition issues are not clearly addressed.

In this section, we document the numerical simulation of an annular self-field thruster. Figure 1 shows a detailed schematic of the axis-symmetric thruster geometry showing dimensions, nodal locations, and region generation scheme. The model employed 8,576 biquadratic elements with velocity, temperature, density, current, magnetic field, and voltage computed at all nine nodes of the element while pressure solution is computed at corner nodes only.

Argon gas propellant enters at temperature T_0, pressure, P_t, mass flow rate $\dot{m}$, and is ionized (within a few millimeters) caused by the applied current density, J_0. Therefore, in this model, the inlet temperature is chosen high enough such that the propellant is sufficiently ionized. As such, the upstream computational boundary is in reality a few millimeters downstream of the true gas entry through the backplate.

3.1 Geometry and Boundary Conditions

Figure 2 show the MPD velocity boundary conditions with zero pressure gradient boundary conditions downstream. Figure 3 show the MPD thermal boundary conditions with an assumed isothermal condition for the inlet and the annode. All other surface have a zero temperature gradient boundary condition which represent an upper bound for thruster operation. Figure 4 show the MPD electromagnetic boundary conditions. We assume the annode and cathode have a constant potential difference, the entry back-plate is electrically insulated, zero downstream axial magnetic field gradients, and magnetic fields are constant at the computational boundary downstream. Although there are other boundary condition combinations, these appear to be ones that are logical and provide physically realistic results.

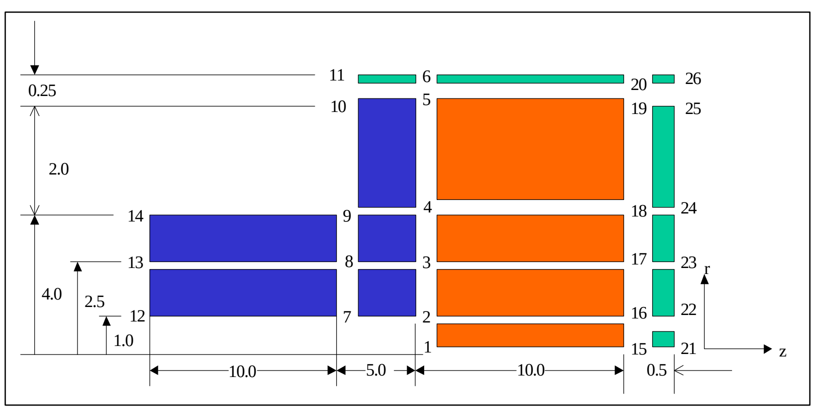

Figure 1. MPD Thruster Geometry (cm)

From Figure 1 the following geometric variables are defined as:

Electrode Length (L_e): 10.0 cm

Inner Radius (R_1): 1.0 cm

Outer Radius (R_2): 4.0 cm

3.2 Plasma Properties

The propellant is Argon gas with the following specified properties and conditions:

Specific Heat Ratio (g): 1.667

Constant Pressure Specific Heat (c_p): 522 J/kg-K

Prandtl Number (p_r): 0.670

Inlet Temperature (T_0): 5,000K

Inlet Pressure (P_t): 1000 Pa

Gas Constant (R_{gas}): 208 J/kg-K

Other property values are computed as follows:

- **Viscosity** :

  Plasma Inlet (Sutherland):

$$m_{f0} = 2.125x10^{-5}\left(\frac{T_0(K)}{273.0}\right)^{0.72} \; Pa-s$$

  Plasma Core:

$$m_f^* = \frac{m_f}{m_{f0}} = \left(\frac{T}{T_0}\right)^{2.5}$$

- **Electrical Conductivity (Spitzer-Harm):**

  Plasma Inlet:

$$s_0 = 1.53x10^{-2}\frac{T_0^{3/2}}{\Lambda(T_0, P_{n_0})} \quad mho/m$$

Plasma Core:

$$s^* = \frac{s}{s_0} = \left(\frac{T}{T_0}\right)^{3/2} \frac{\Lambda(T_{0,}P_{n_0})}{\Lambda(T, P_n)}$$

$$\Lambda(T, P_n) = 23 - \ln\left[\frac{1.22x10^3 P_n^{0.5}}{T^{3/2}}\right]$$

$$P_n(r) = \frac{r\left(kg/m^3\right)}{6.68x10^{-26}kg}$$

- **Thermal Conductivity**

Plasma Inlet:

$$k_0 = \frac{m_{f_0} c_p}{pr} \quad W/m-K$$

Plasma Core*:*

$$k^* = \left(\frac{T}{T_0}\right)^{5/2} \frac{\Lambda(T_0, P_{n_0})}{\Lambda(T, P_{n)}}$$

- **Density**:

Plasma Inlet:

$$r_0 = \frac{P_t}{R_{gas} T_0} \quad kg/m^3$$

4.0 MPD Thruster Simulation Results

An overall schematic for the MPD algorithm is provided in [8]. The algorithm employs 9-node quadrilateral finite elements with the following modeling parameters:

Elements: 8,576 9-node Quadrilateral Elements

Nodes: 34,412

DOF: 147,849 $\{v_z, v_r, T, r, P\}$

137,648 $\{J_z, J_r, B_q, f\}$

Wave Front: 895

The convergence parameter is defined as the *Residual Norm* expressed as:

$$\bar{R} = \frac{\sum_0^n \left| \left(Y^{m+1} - Y^m \right) \right|}{\sum_0^n \left| Y^m \right|} \leq 10^{-5}$$

where Y is the individual nodal degree of freedom, 'm' is the iteration index, and where the sum is over all nodal degrees of freedom. Figures 5 and 6 show the fluid dynamics and electromagnetics equations convergence history, respectively, for a mass flow rate of 2 gm/s and a current of 4,000 amps. Note the rather stable computational behavior of the both the GFEM and the LSFEM algorithms. Additional sample results are provided in Figures 7-10 that show contour plots for Speed, temperature, Density, and Voltage, respectively. Results are shown for a mass flow rate of 2.25 gm/s and a current of 4,000 amps. Note the temperature increase along the insulated cathode surface and the velocity increase within a narrow region above the cathode surface. This velocity increase corresponds to the location of the maximum induced magnetic field (i.e. along the cathode surface). Also note the velocity decrease in the plasma core downstream of the inlet due to mass conservation. Observe the exit velocity increase due to heat transfer from the cathode to the anode. This heat transfer provides increased density and a corresponding increased convective fluid acceleration. Finally, the increased density creates density gradients that provide additional axial and radial momentum thrust forces.

Although not shown, the induced magnetic field has a maximum value along the cathode surface associated with a maximum radial current density. The larger cathode temperature and the associated temperature dependent electrical conductivity result in this maximum radial current density.

4.1 Parametric Studies

To evaluate the system performance the total thrust is defined as:

$$T_e = \dot{m}v_e + \int_{V_{ext}} (\vec{J}\times\vec{B})dV_{ext} + \int_{A_e} p(r)dA_e - p_t A_e$$

where the integration of the electromagnetic body force is performed over the current carrying volume ‘***external’*** to the thruster (V_{ext}). This is necessary due to possible electromagnetic accelerations that may occur outside the thruster. The pressure force corresponds to an imbalance between the pressure at the anode exit plane (p_e) and the background gas pressure (p_t) evaluated over the thruster exit area A_e.

The total thrust is now used to calculate the plasma flow efficiency:

$$h_f = \frac{T_e^{\,2}}{2\dot{m}P}$$

where P is the power deposited in the plasma, equal to the product of the plasma voltage and the plasma resistivity, i.e.

$$P = \frac{I_0^2}{s_0}.$$

Unfortunately, due to significant electrode power losses that consume a large fraction of the total thruster power, experimentally measured thruster efficiencies will be lower [19]. However, the finite element model can provide trends, parametric studies, and design comparisons.

Plots of exit thrust, density, and temperature are shown in Figures 11, 12, and 13 respectively for $\Psi_0 = 1$ (*ratio of electrical input power to thermal input power*). The maximum thrust occurs at a radial distance of 3 cm (Figure 11) with a corresponding density maximum (Figure 12) and a corresponding temperature minimum (Figure 13) slightly less that 3cm. Note the “flat” temperature profile between radial values of 3-4cm and the slight temperature increase prior to the upper boundary at 4.0 cm. This affect is also reflected in the exit density plot and is attributed to the coupling of density, temperature, and velocity within the element stiffness matrix. Negative density gradients reduce the local velocity and the corresponding convective heat transfer toward the upper radial boundary.

4.2 Understanding Y

The dimensionless parameter $\underline{\Psi}$ is analogous to the physical parameter I^2/m used to compare MPD thrusters. For constant Ψ, and constant I^2/m, the thrust and efficiency increases with increasing current (Figure 14) as expected. For constant current and varying Ψ (or varying I^2/m) the efficiency increases with increasing mass flow and resulting increased thrust as expected (Figures 15,16). Finally, Figure 17 shows that a decreasing Ψ results in higher flow efficiencies and Figure 18 shows that increasing current result in higher flow efficiency for constant Ψ. These trends are consistent with other simulations provided within the literature [2].

However, for constant mass flow (m) and increasing current (I), the thrust and efficiency <u>decreases</u> with increasing current. Although this appears strange, an analysis of the formulation provides two possible explanations:

1. The non-dimensionless parameters Δ, which controls the Magnetohydrodynamics momentum body force, and Ψ, which controls the Magnetohydrodynamics Joulean heating load within the energy equation, both vary as I^2 for this case. Although both increase, negative momentum density gradients retard the developing axial velocity (Equation 8), and therefore reduce thrust and efficiency.
2. The increase in the Joulean heating is offset by the convective heat transfer increase. This result in cooler cathode temperatures and small density gradients combined with lower thrust and efficiency.

It is clear that additional research is needed to understand this result.

We also define the "*conversion*" efficiency as:

$$b = \frac{(T_e)(V_e)}{Q_0} \tag{13}$$

where the numerator is the mechanical thrust power at the exit plane and the denominator is the reference plasma thermal power at the inlet. Figure 19 shows the current vs. conversion efficiency for constant Ψ. Note that for increasing current and decreasing Ψ, the conversion efficiency increases. This result follows from the increased reference magnetic velocity and the decreased reference magnetic force ratio, Δ_0. A smaller magnetic force ratio subsequently results in increased convective acceleration and increased convective heat transfer due an increased Peclect number. The increased convection of momentum and energy creates larger temperature and density gradients and as such, increased thrust and conversion efficiency.

Conclusions

This paper presents a loosely-coupled single-fluid and single temperature MHD algorithm that combines the traditional Galerkin Finite Element Method and the Least Square Finite Element

Method. The algorithm has good convergence properties, is very stable for typical MPD operating conditions, and is applicable for steady compressible Magnetohydrodynamics fluid flow with heat transfer, assuming a fully ionized plasma.

Additionally, the Least Square Finite Element Method provides a framework for a unified approach applicable to interdisciplinary problems in fluid dynamics. This method is based upon a first-order differential equation formulation. Using C^0 finite elements to discretize the equations and minimize the L_2 norm of the residuals leads to a symmetric and positive-definite algebraic system that can be effectively solved by simple yet robust matrix-free iterative methods. Furthermore, using an Element-by-Element (EBE) Preconditioned Conjugate Gradient (PCG) approach will allow algorithm development that does not require the assembly of the global <u>or</u> local elemental stiffness matrices. This characteristic can effectively be utilized for the solution of large-scale problems on parallel computers.

We also presented a non-dimensional numerical formulation that provides insight into fundamental parameters governing MPD thrusters. As a result we propose the "PSI" factor (Ψ) along with the conversion efficiency β as dimensionless parameters to compare MPD thrusters. Ψ_0 along with the applied current, reference temperature, geometry data, and fluid property data is sufficient for the parametric analysis of MPD thrusters.

Modeling improvements for increased accuracy are:

- An Equation of State (EOS) for real fluids
- Transient Simulations
- Temperature dependent specific heats
- Inclusion of a two component model for ions and electrons
- Radiation effects

We anticipate these modeling improvements will be very useful when combined with geometry optimization algorithms to study thruster geometry affects on efficiency.

References

1. F.M. White, *Viscous Fluid Flow*, McGraw Hill, 1974.
2. W.F. Hughes and F.J. Young, *The Electromagnetodynamics of Fluids*, John Wiley, 1966.
3. P.P. Lynn and S.K. Arya, “Use of least square criterion in the finite element formulation,” Int. Journal of Numerical Methods in Engineering, Vol. 6, pp. 75-88, 1973.
4. Baker, A.J., J. Iannelli, D.J. Chaffin and S. Roy, “Some recent adventures into improved finite element CFD methods for convective transport,” Computer Methods in Applied Mechanics and Engineering, Vol. 151, pp. 27-42, 1998.
5. G.J. Fix and M.E. Rose, A Comparative study of Finite Element and Finite Difference Methods for Cauchy-Rieman Type Equations, SIAM J. Numer. Anal, 22 (1985), 250-260.
6. Bo-Nan Jiang and L.A. Povinelli, Least_Squares Finite Element Method for Fluid Dynamics, Comp. Methods Applied Mechanics and Engrg, 81 (1990), 13-37.
7. B.-N. Jiang and L.-J. Hou, T.L. Lin and L.A. Povinelli., Least-Squares Finite Element Solutions for Three-Dimensional Backward-Facing Step Flow, Comp. Fluid Dyn., 4 (1995), 1-19.
8. K.J. Berry, and S. Roy, Least Square FE Based MPD Algorithm for Practical Magnetoplasma Applications, AIAA 39th Aerospace Sciences Meeting, AIAA-2001-0200, Jan. 2001.
9. F.F. Chen, Plasma Physics and Controlled Fusion, Plenum Press, 1984.
10. D.E. Hastings and E.H. Niewood, “Theory of the modified two-stream instability in a magnetoplasma-dynamic thruster,” Journal of Propulsion and Power, Vol. 7, No. 2, pp. 258-268, 1991.

11. E.Y. Choueiri, *Electron-ion Streaming Instabilities of an Electromagnetically Accelerated Plasma*, PhD dissertation, Princeton University, 1991.

12. M. Lapointe, “Numerical simulation of self-field MPD thrusters,” AIAA Paper No. 91-2341, 1991.

13. P.C. Sleziona, M. Auweter-Kurtz and H.O. Schrade, “Computation of MPD flows and comparison with experimental results,” Int. Journal for Numerical Methods in Engineering, Vol. 34, pp. 759—771, 1992.

14. H. Kawaguchi, K. Sasaki, H. Itoh, and T. Honma, “Numerical study of the thrust mechanism in a two-dimensional MPD thruster,” Int. Journal of Applied Electromagnetics and Mechanics, Vol. 6, pp. 351--365, 1995.

15. M. Auweter-Kurtz, C. Boie, H.J. Kaeppeler, H.L. Kurtz, H.O. Schrade, P.C. Sleziona, H.P. Wagner and Th. Wegmann, “Magnetoplasmadynamic thrusters: design criteria and numerical simulation,” Int. J. of Applied Electromagnetics in Materials, Vol. 4, pp. 383-401, 1994.

16. R.E. Peterkin, M.H. Frese, and C.R. Sovinec, “Transport of magnetic flux in an arbitrary coordinate ALE code,” Journal of Computational Physics, Vol. 140, pp. 148-171, 1998.

17. P.G. Mikellides and P.J. Turchi, “Applied-field magnetoplasmadynamic thrusters, Part 1: Numerical simulations using the MACH2 code,” Journal of Propulsion and Power, Vol. 16, No. 5, pp. 887-893, 2000.

18. L.Q. Tang and T.T.H. Tsang, Transient Solutions by a Least-Squares Finite-Element Method and Jocob Conjugate Gradient Technique, Numerical Head Transfer, 28 (1995), 183-198.

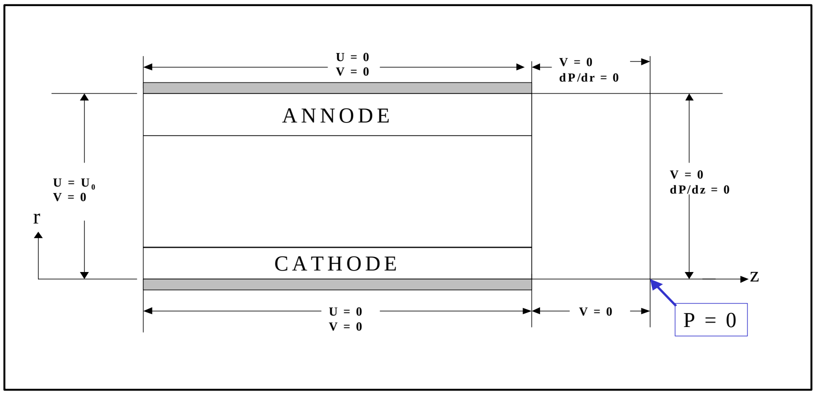

Figure 2. MPD Velocity Boundary Conditions

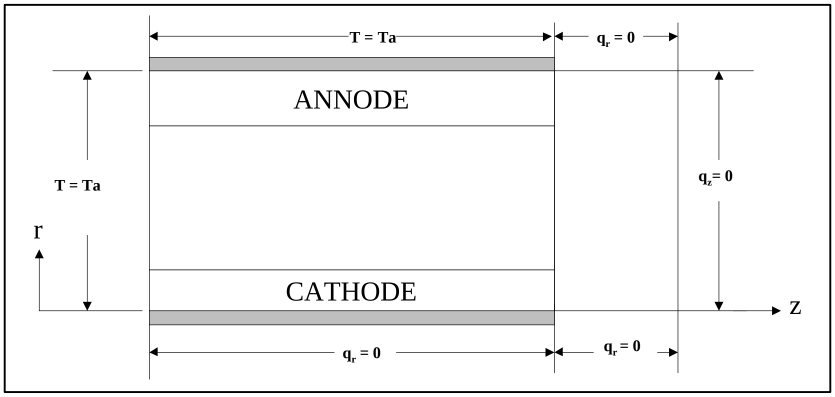

Figure 3. MPD Thermal Boundary Conditions

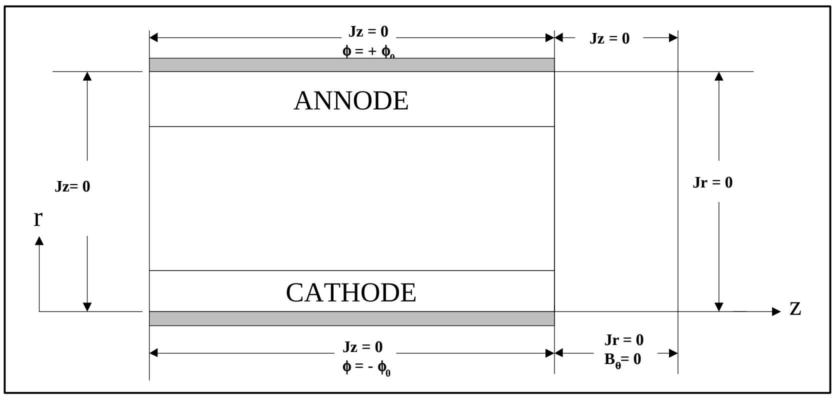

Figure 4. MPD Electromagnetic Boundary Conditions

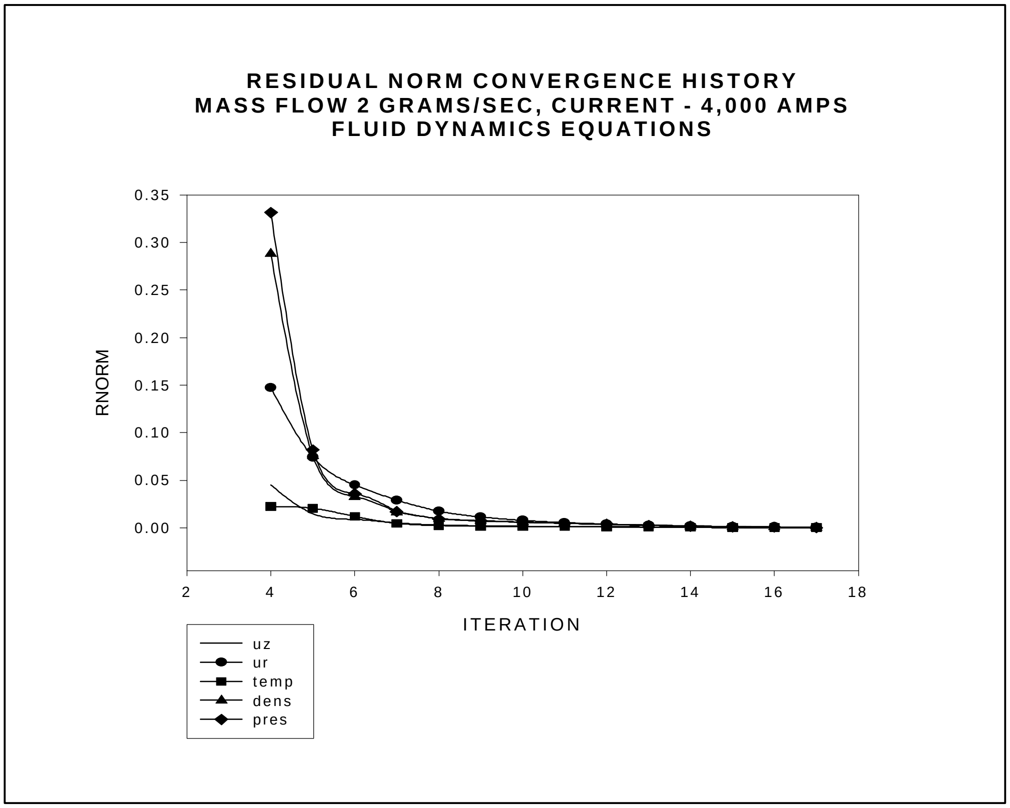

Figure 5. Residual Norm Convergence History – Fluid Dynamics

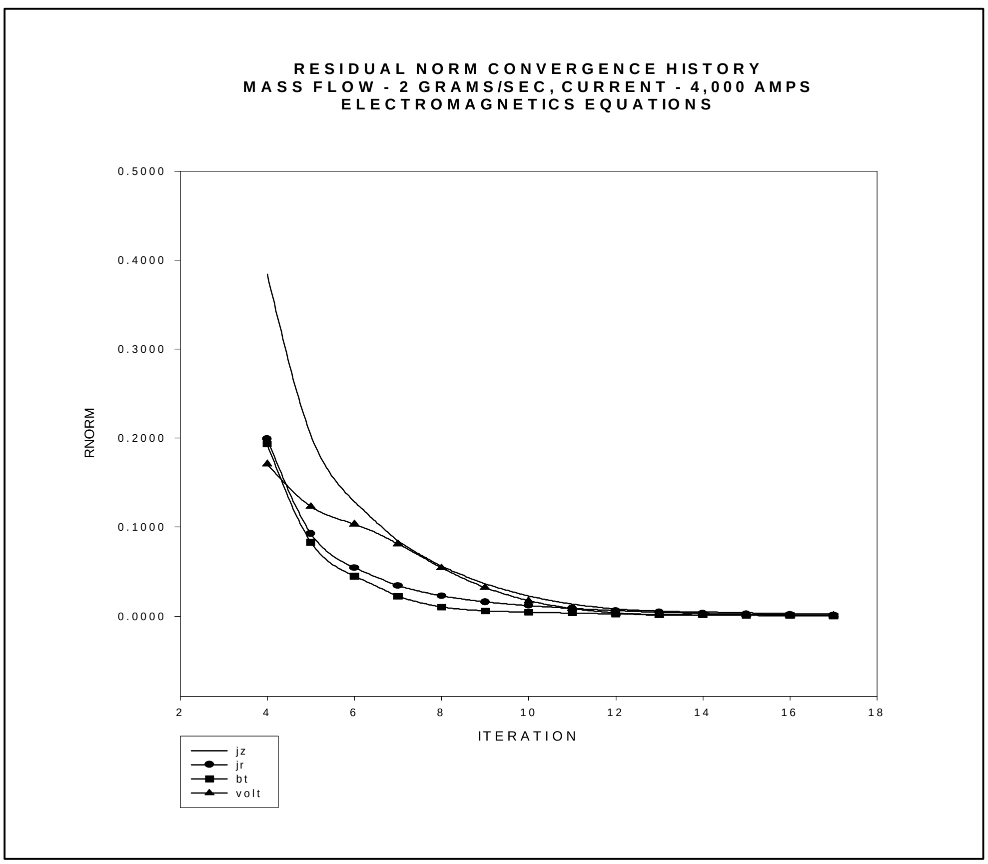

Figure 6. Residual Norm Convergence History – Electromagnetics

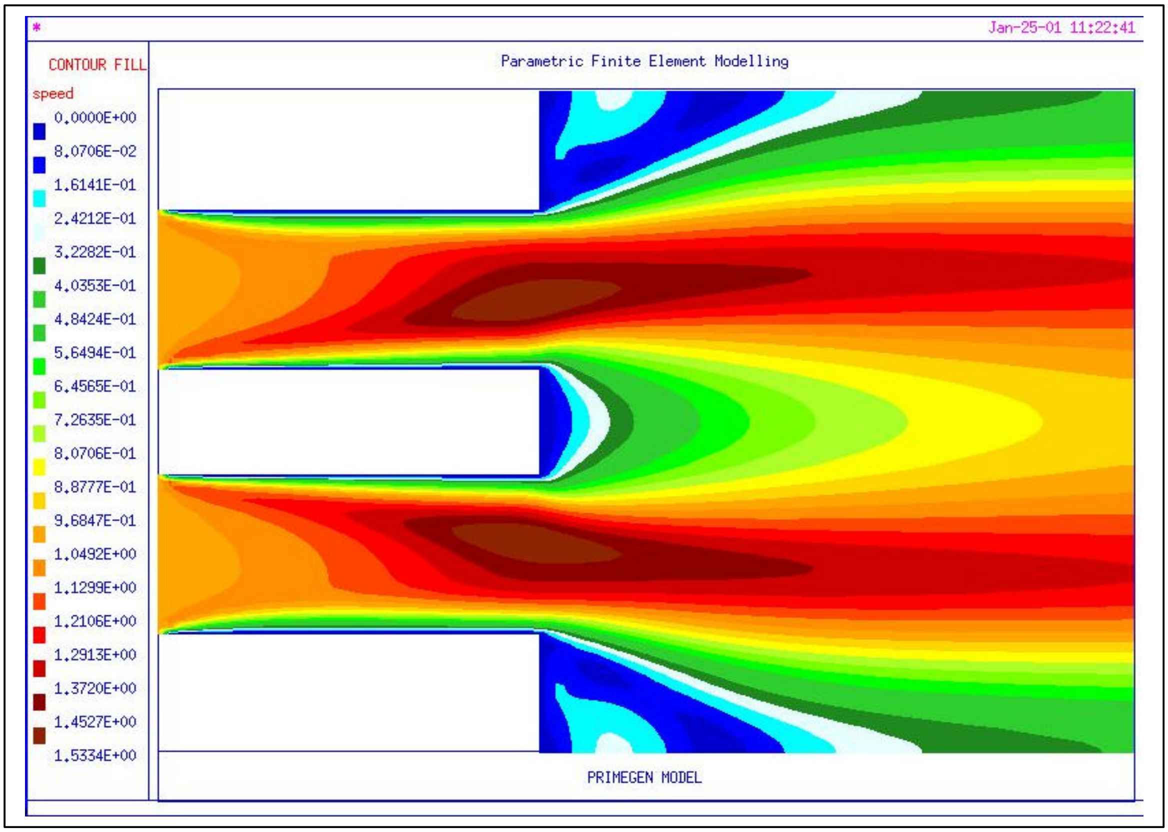

Figure 7. Contour Speed Plot

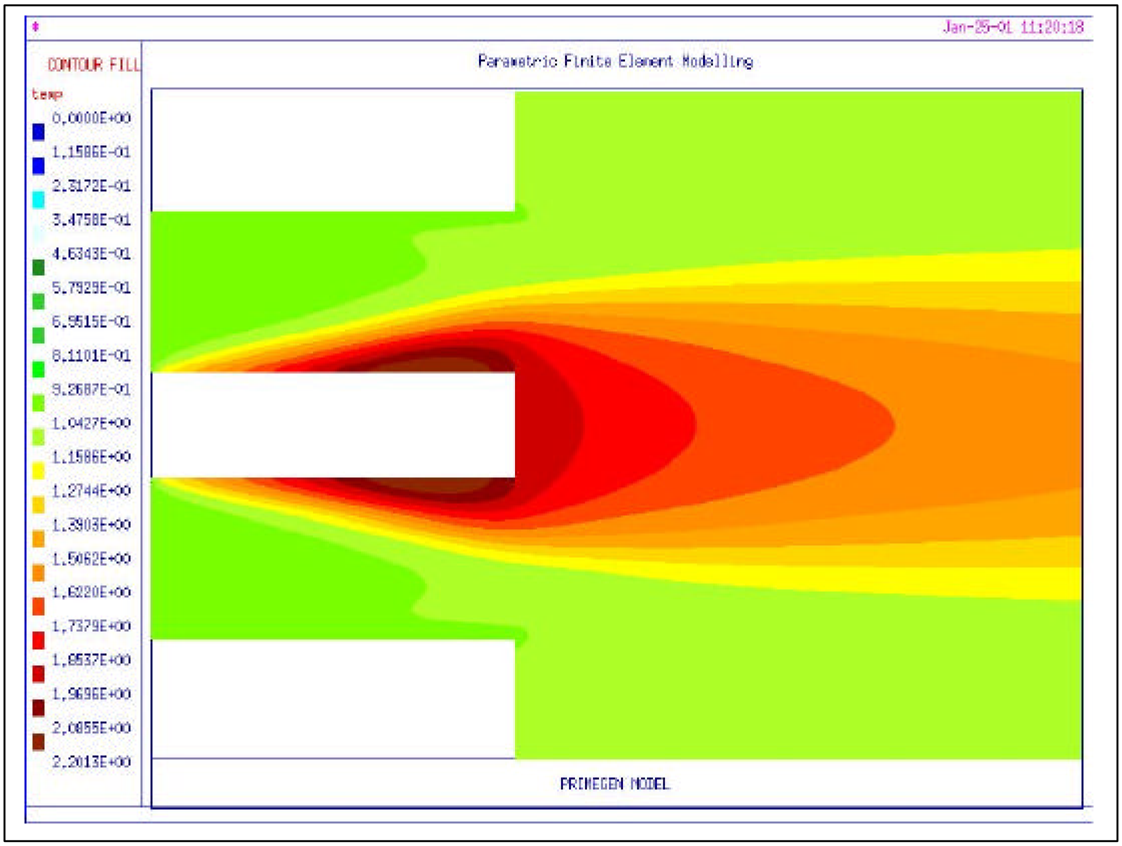

Figure 8. Contour Temperature Plot

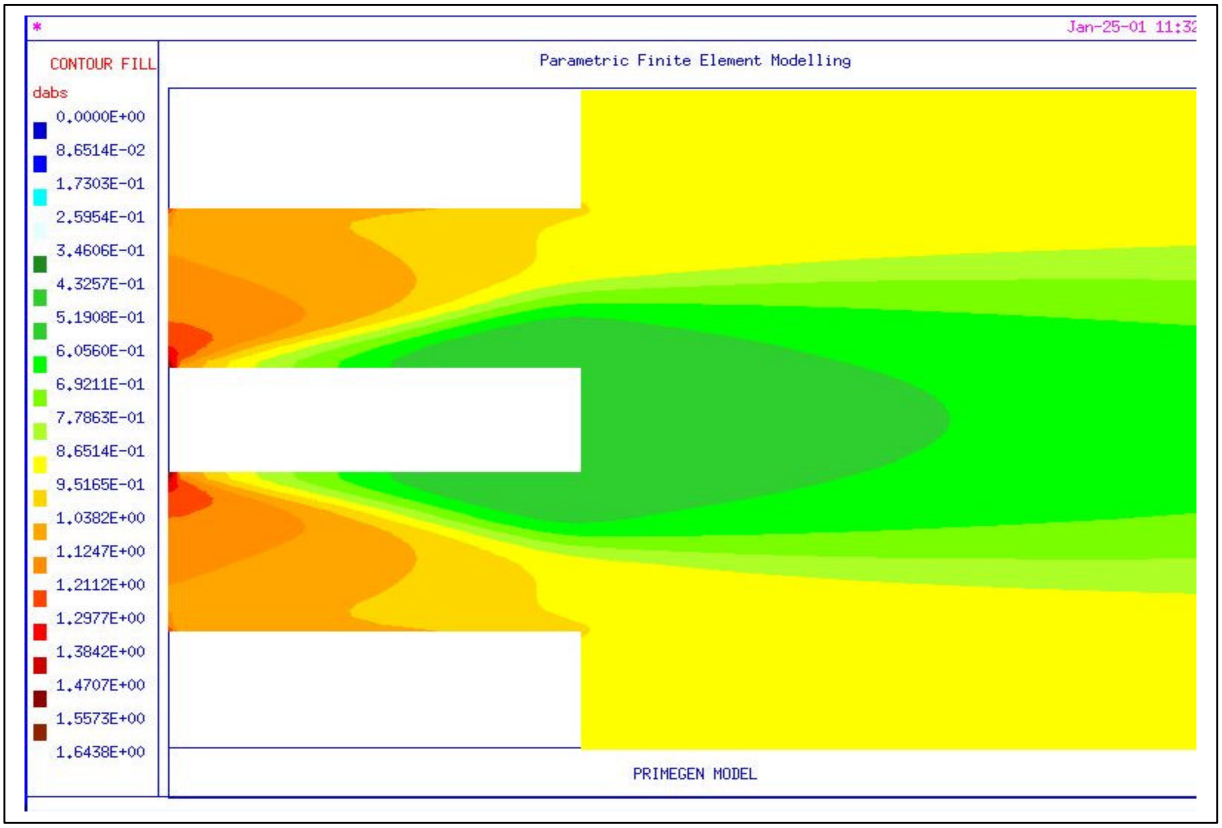

Figure 9. Contour Density Plot

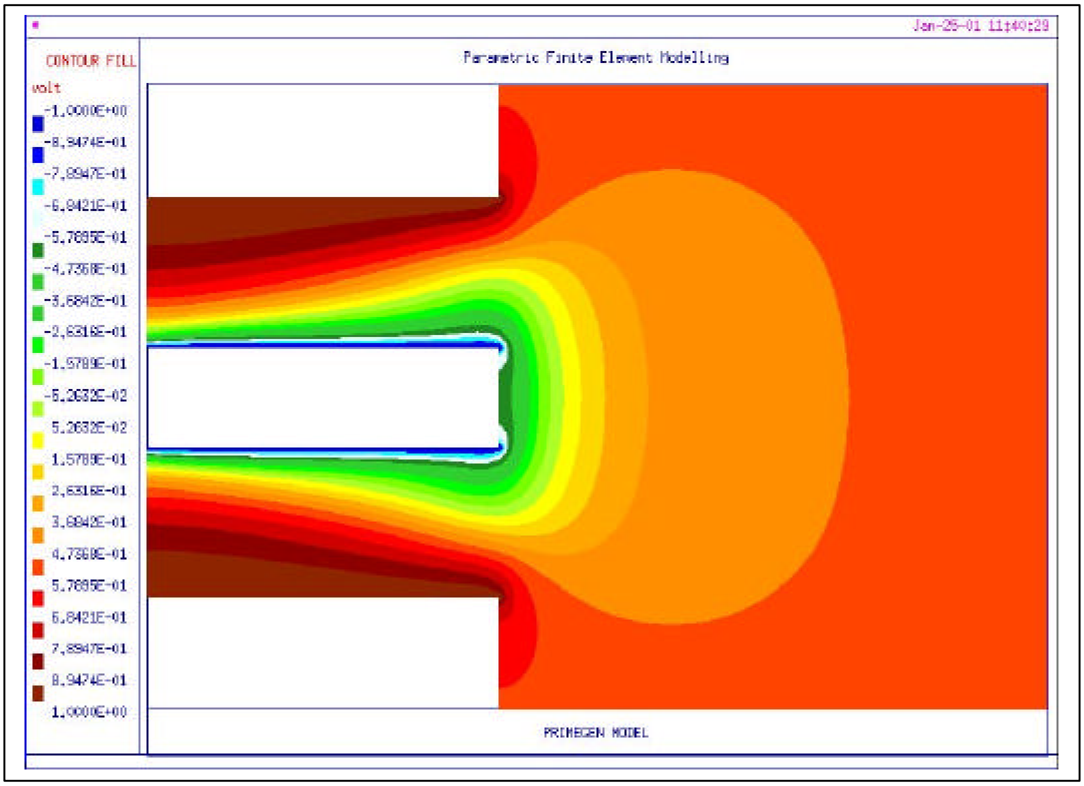

Figure 10. Contour Voltage Plot

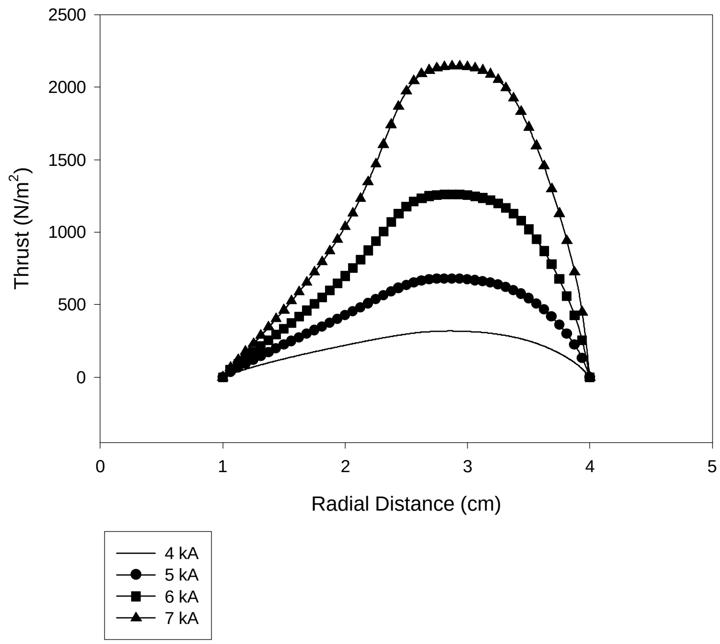

Figure 11. Exit Thrust vs. Current

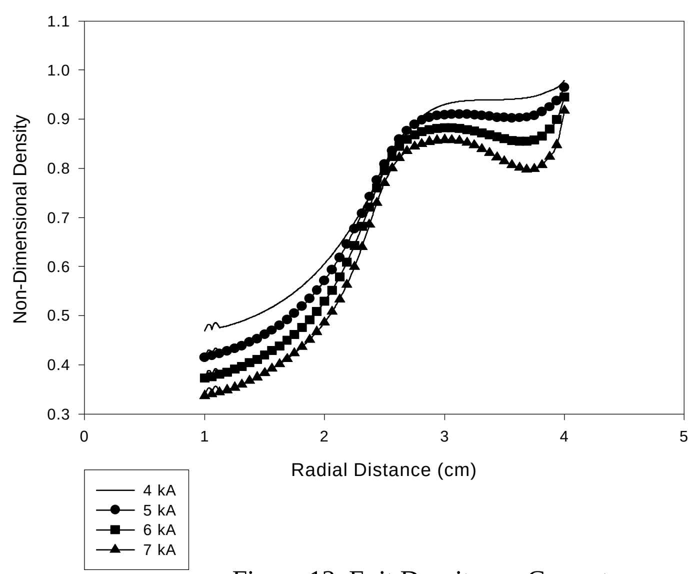

Figure 12. Exit Density vs. Current

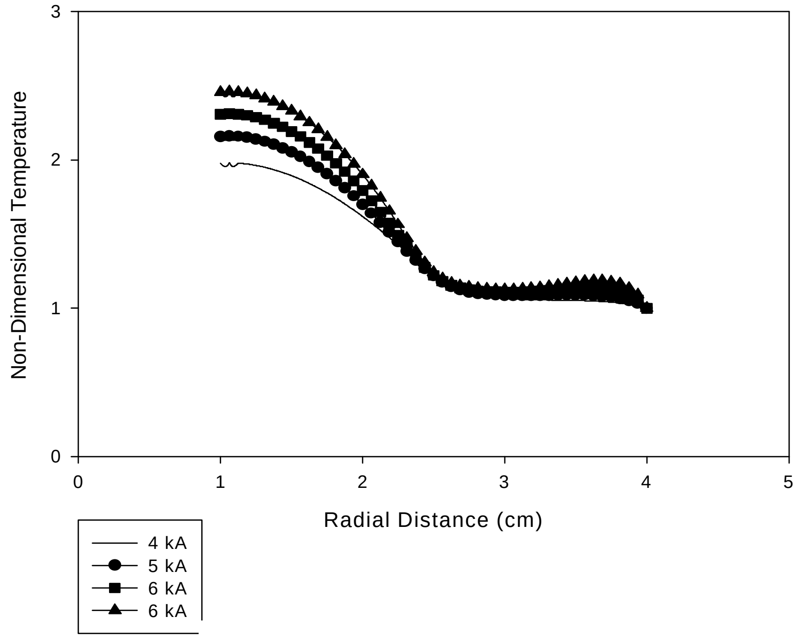

Figure 13. Exit Temperature vs. Current

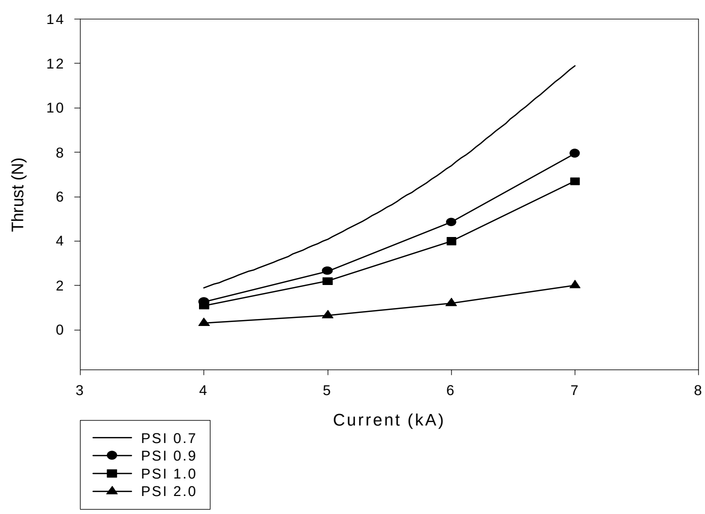

Figure 14. Current vs. Thrust

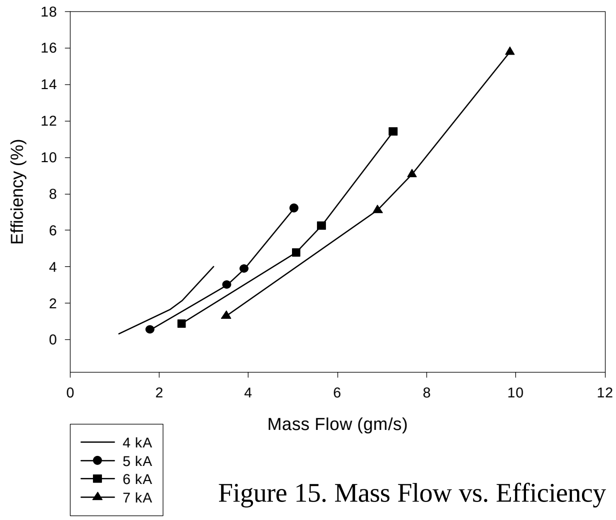

Figure 15. Mass Flow vs. Efficiency

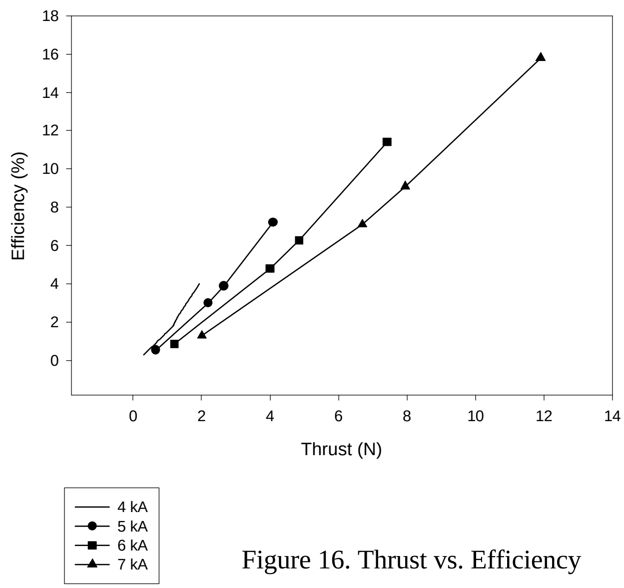

Figure 16. Thrust vs. Efficiency

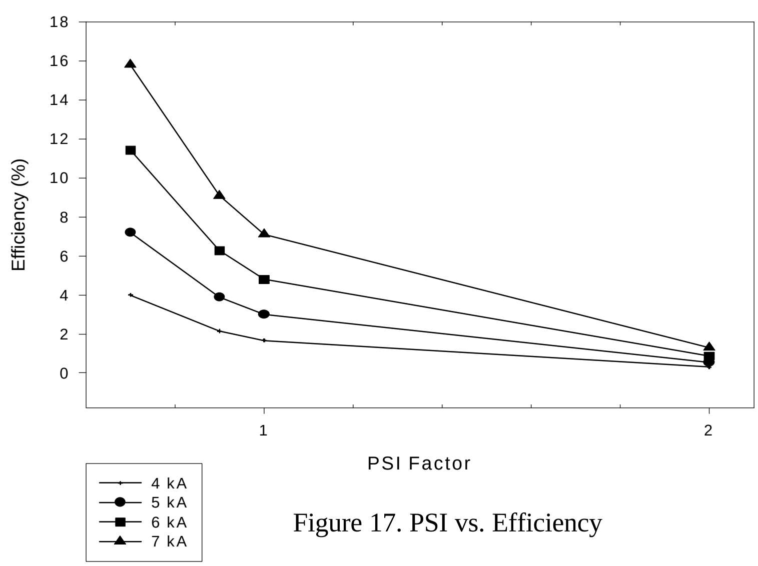

Figure 17. PSI vs. Efficiency

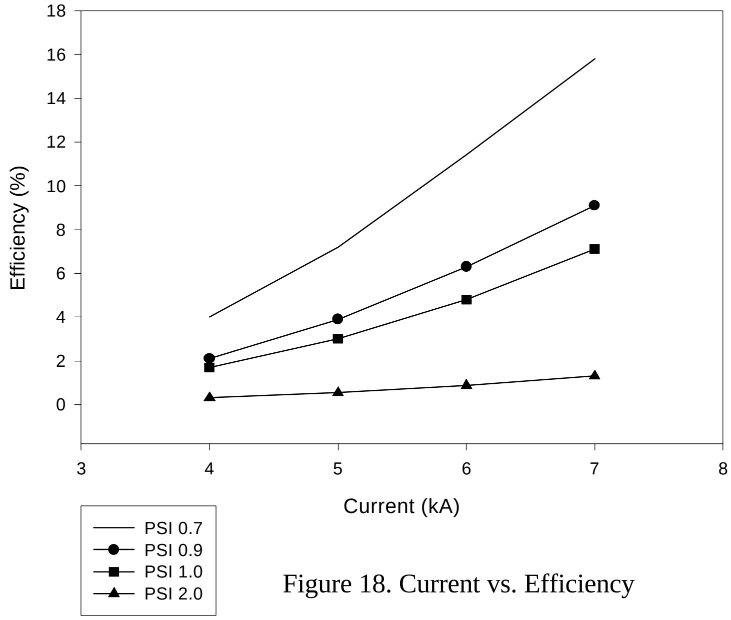

Figure 18. Current vs. Efficiency

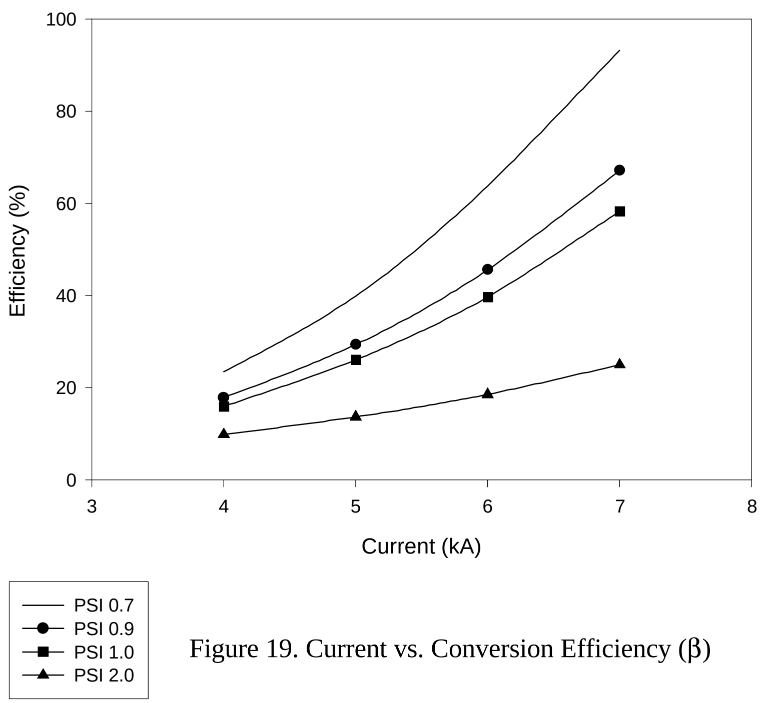

Figure 19. Current vs. Conversion Efficiency (β)